Silicone Oil-Induced Glaucomatous Neurodegeneration in Rhesus Macaques

Ala Moshiri[1,5], Fang Fang[2,3,5], Pei Zhuang[2,4], Haoliang Huang[2], Xue Feng[2], Liang Li[2], Roopa Dalal[2], and Yang Hu[2,*]

[1]Department of Ophthalmology & Vision Science, School of Medicine, University of California Davis, Sacramento, CA 95817, USA.

[2]Department of Ophthalmology, Stanford University School of Medicine, Palo Alto, CA 94304, USA

[3]Department of Ophthalmology, The Second Xiangya Hospital, Central South University, Changsha 410011, China

[4]Current address, Janssen Research & Development, South San Francisco, CA 94080, USA

[5]These authors contributed equally.

* Correspondence and requests for materials should be addressed to Y.H. (huyang@stanford.edu)

Abstract

Previously, we developed a simple procedure of intracameral injection of silicone oil (SO) in mouse eyes and established the mouse SOHU (SO-induced ocular hypertension) glaucoma model with reversible intraocular pressure (IOP) elevation and significant glaucomatous neurodegeneration (Zhang et al, eLife 2019). Because the anatomy of the non-human primate (NHP) visual system closely resembles that of humans, it is the most likely to predict human responses to diseases and therapies. Here we replicated the SOHU glaucoma model in rhesus macaque monkeys. One animal presented characteristic human glaucoma pathophysiological features within 6 months after SO injection, including reversible IOP elevation, optic nerve head (ONH) cupping, quadrant specific RNFL thinning, and decrease of the photopic negative response, in addition to significant retinal ganglion cell (RGC) death and optic nerve (ON) degeneration. Additional animals showed similar glaucomatous degeneration and visual functional deficit at both 3 and 6 months, however, with a unique dynamic change of IOP. This novel NHP SOHU glaucoma model recapitulates phenotypes of human patients, and is therefore highly suitable for studying primate RGC/ON morphology and function in response to ocular hypertension, assessing pre-clinically neuroprotective and regenerative therapies, and therefore for translating relevant findings into novel and efficient treatments in patients with glaucoma and other neurodegenerations.

Keywords: glaucoma, retinal ganglion cell, optic nerve, neurodegeneration, model, NHP

Introduction

Glaucoma, the most common cause of irreversible blindness, is characterized by progressive peripheral to central loss of retinal ganglion cells (RGCs) and their axons in optic nerve (ON) (Calkins, 2021; Howell et al., 2007; Tham et al., 2014; Weinreb et al., 2016). Although glaucoma can occur at any intraocular pressure (IOP) level (Iyer et al., 2020), elevated IOP is associated with accelerated progression (Burgoyne, 2011; Calkins, 2012; Calkins, 2021; Howell et al., 2007; Tham et al., 2014; Weinreb et al., 2016). Lowering IOP is the only available treatment but fails to completely prevent the progression of glaucomatous neurodegeneration (Anderson and Normal Tension Glaucoma, 2003; Garway-Heath et al., 2015; Heijl et al., 2002; Wormald et al., 2020). Neuroprotectants that promote RGC/ON survival, transplantation of stem cell-derived RGCs to replace lost RGCs, and regeneration therapies to stimulate RGC soma and axon regrowth are promising neural repair strategies to restore vision in glaucoma patients (Beykin et al., 2021; Wareham et al., 2020). To translate exciting laboratory findings into effective neuroprotective and regenerative treatments, pre-clinical testing in a disease-relevant, translation-enabling animal glaucoma model that closely resembles human patients is critically important.

We recently developed a silicone oil (SO)-induced ocular hypertension (SOHU) glaucoma mouse model (Fang et al., 2021; Zhang et al., 2019a; Zhang et al., 2019b) based on the well-documented, SO-induced human secondary glaucoma that occurs as a complication of vitreoretinal surgery (Ichhpujani et al., 2009; Kornmann and Gedde, 2016). By thwarting aqueous flow to the anterior chamber with a single intracameral injection of SO and that induces pupillary block, this model causes accumulation of aqueous and significant IOP elevation in the posterior chamber, and subsequent progressive RGC and ON degeneration. Importantly, the ocular hypertension of SOHU

model can be reversed quickly by easily and definitively removing SO from the anterior chamber (Fang et al., 2021; Zhang et al., 2019a; Zhang et al., 2019b). However, there is a recognized gap in the translation of successful neuroprotective and regenerative therapies identified in rodent models of glaucoma to treatment for glaucoma patients. Rodents have known limitations that may impede translation of potential therapeutics: differences in immune system responses, ON head (ONH) architecture, and brain structures and circuitry may contribute to differences in pathogenesis between rodents and primates and, therefore, to critically different responses to therapeutics. Therefore, despite the many benefits of the mouse SOHU model, a higher experimental animal species is needed for pre-clinical translation research.

The anatomy of the non-human primate (NHP) visual system closely resembles that of humans and includes a similar distribution of rods and cones, a specialized macula and fovea and lamina cribrosa not present in rodent, comparable contrast sensitivity and visual acuity, and almost identical retinocortical architecture (Chen et al., 2016; Harwerth and Smith, 1985). An NHP glaucoma model is the most likely to predict human responses to ocular hypertension and therapies, and the rhesus macaque monkey has been used successfully in experimental glaucoma research (Burgoyne, 2015a; Burgoyne, 2015b). Since SO causes ocular hypertension in both human patients and mice, we reasoned that the same procedure may be adapted to different animal species with minimal confounding factors. Here we report the development of a novel NHP glaucoma model in rhesus macaque monkeys by adapting our mouse SOHU glaucoma model. By characterizing the unique features of SO-induced IOP dynamics in macaque eyes and the corresponding RGC/ON degeneration and visual function deficits, we provide essential information to establish the NHP SOHU glaucoma model. We expect this model to be applicable

87 to study primate RGC morphology and function in response to ocular hypertension, and assess
88 pre-clinically promising neuroprotective and regenerative therapies, and therefore for translating
89 relevant findings into novel and efficient treatments in patients with glaucoma and other
90 neurodegenerations.

91

92

93 **Results**

94 **Intracameral injection of SO in rhesus macaque monkey produces characteristic**
95 **pathophysiological features of human glaucoma**

96 We injected roughly 100 µl SO into the anterior chamber of the right eye of one 13-year-old female
97 macaque (#38361, **Table 1**), filling 80% SO of the anterior chamber with complete covering of
98 the pupil (**Fig. 1A**). The IOPs of both eyes were similar before SO injection (Day 0, 17 *vs* 16
99 mmHg, **Fig. 1B**). Restrictions of the Primate Center then precluded measuring the IOPs until 1
100 month post injection (1mpi). Surprisingly, the IOP of the SOHU eye was lower at this time than
101 the contralateral mock injected control eye (10 *vs* 19 mmHg). However, significant elevation of
102 IOP was detected at 3 and 5mpi in the SOHU eye (**Fig. 1B**). Because we missed the measurement
103 at the 2mpi time point, we can only assume that the IOP of the SOHU eye recovered and became
104 elevated between 1mpi and 3mpi. Consistent with our mouse SOHU model, SO removal at 5mpi
105 reduced IOP dramatically at 1 week after SO removal, the earliest time point we measured, and it
106 had returned to normal at one month after SO removal (6mpi) (**Fig. 1B**). These results indicate that
107 the SO-induced pupillary blocking was the cause of IOP elevation, and that the pupillary blocking
108 and ocular hypertension were reversed by simply removing the SO.

109

110 A characteristic morphological feature of human glaucoma is enlargement of the depression in the
111 middle of the ONH, called glaucomatous "cupping" (Lockwood et al., 2015; Yang et al., 2017).
112 Strikingly, this signature morphological change of glaucoma was readily detected in the SOHU
113 macaque eye by live fundus imaging with confocal scanning laser ophthalmoscopy (cSLO) at 3
114 and 5mpi (**Fig. 1C**), corresponding to IOP elevation. ONH cupping cannot be seen in the mouse
115 SOHU model, further confirming the similarity between macaque and human eyes.

116

117 This characteristic glaucomatous optic cup enlargement was even more obvious in OCT live
118 imaging by radial B-scan centered through the ONH (**Fig. 2A**). Based on previously developed
119 measurement of the anatomic features of the macaque ONH (He et al., 2014; Yang et al., 2017),
120 we applied the Visualization Toolkit (VTK) to generate an algorithm for 3D reconstruction to
121 delineate the OCT imaging data (**Fig. 2B**). We used inner limiting membrane (ILM), Bruch's
122 membrane opening (BMO), the two discrete points at either side of the neural canal, and the BMO
123 reference plane as references to measure the ONH connective tissue parameters, including
124 minimum rim width (MRW), rim volume (RimV), and cup volume (CupV). Obvious shortening
125 of MRW, shrinking of RimV, and enlarging of CupV were detected in the SOHU eye compared
126 to contralateral control eye (**Fig. 2C**).

127

128 Thinning of the retina nerve fiber layer (RNFL) measured by OCT is used clinically as a biomarker
129 for RGC/ON degeneration (Aktas et al., 2016; Balcer et al., 2015; Costello et al., 2006). We
130 measured the RNFL thickness of this animal sequentially and detected a progressive decrease from
131 1mpi to 6mpi (**Fig. 3**), indicating significant glaucomatous neurodegeneration. Interestingly,

132 RNFL thinning was more severe in the inferior and superior quadrants, as in human glaucoma
133 (Maupin et al., 2020). Additionally, we detected a retinal branch artery occlusion in the SOHU
134 eye with corresponding temporal inner retinal thinning in the macular region (**Figure 3-figure**
135 **supplementary 1**), which significant IOP elevation can also cause in human patients (Varma et
136 al., 2013).
137
138 We also examined the visual function of this macaque. The photopic negative response (PhNR) of
139 the photopic full-field ERG is a negative-going wave that occurs after the b-wave in response to a
140 brief flash and reflects the function of RGCs and their axons in general. Its amplitude is reduced
141 early in human glaucoma (Viswanathan et al., 1999), which also correlates well with structural
142 loss in NHP glaucoma (Wilsey et al., 2017). Both b-wave and PhNR's amplitudes decreased
143 dramatically in the SOHU eye at 1-6mpi, suggesting functional deficits of the inner retina (**Fig. 4**).
144
145 Finally, to confirm the glaucomatous neurodegeneration, we euthanized this animal at 6mpi for
146 histological analysis of post-mortem retina and ON. Consistent with the structural and functional
147 deficits detected in the living animal, retinal wholemounts revealed significant RGC somata loss
148 in the SOHU eye throughout the peripheral to the central retina (**Fig. 5A,B**); and semithin cross-
149 sections showed significant RGC axon degeneration in ON (**Fig. 5C,D**). The H&E staining of the
150 ONH further confirmed the "cupping" phenotype and significant thinning of RNFL (**Figure 5-**
151 **figure supplementary 1A**). The lamina cribrosa is a three-dimensional trabecular connective
152 tissue providing structural support and load-bearing to RGC axons at the ONH (Downs and Girkin,
153 2017). Its deformation, such as increased curve and depth, may correlate with RNFL thinning in
154 glaucoma patients (Hopkins et al., 2020; Kim et al., 2018). Interestingly, collagen staining of the

155 ONH of the SOHU eye also showed lamina cribrosa bowing (**Figure 5-figure supplementary**
156 **1B**).
157
158 Taken together, results in this rhesus macaque monkey (#38361) not only replicated the mouse
159 SOHU glaucoma model in NHP, but also demonstrated characteristic pathophysiological features
160 of human glaucoma, including ONH cupping, quadrant specific RNFL thinning and significantly
161 decrease of visual function (PhNR), confirmed by histological studies showing significant RGC
162 death and ON degeneration.
163
164
165 **Acute form of macaque SOHU model with different IOP dynamics but similar**
166 **neurodegeneration in most tested animals**
167 Five of the other tested macaques (**Table 1**) showed different IOP dynamics after SO injection
168 than animal #38361. In two animals (#44876 and #45513), IOP was elevated immediately after
169 SO injection (15 to 19 mmHg and 13 to 22 mmHg, **Fig. 6A**). Due to the pandemic and strict
170 regulation of the Primate Center, we could not measure the IOP at earlier time points or more
171 often. We do not know for how long the transient IOP elevation after SO injection lasts. However,
172 all the 5 animals showed substantial ocular hypotension at 1mpi: IOPs of the SOHU eyes were
173 much lower than their baselines or their contralateral control eyes (**Fig. 6A,B**). The ocular
174 hypotension lasted from 1mpi to 3mpi in three animals (#44876, #45513, and #44639), and IOP
175 returned progressively to normal between 2-6mpi in the other three animals that we maintained for
176 6 months. We do not know whether the IOPs of these SOHU eyes will become elevated again after
177 the 6mpi time point. We noticed that all the pupils of the SOHU eyes were fixed in the mid-dilated

178 state (**Fig. 7A**), suggesting a transient and quick IOP elevation, which may result in ischemic iris
179 sphincter muscle and consequently limitation in constriction, as in patients with acute angle closure
180 glaucoma (Flores-Sanchez and Tatham, 2019). Similarly, the chronic ocular hypotony may be the
181 result of acute IOP elevation and subsequent ischemia of the ciliary body. Consistent with low
182 IOP, neither retina fundus SLO images nor OCT images showed ONH "cupping" (**Figs. 7B,C**).

183

184

185 **Significant neurodegeneration of the SOHU eyes at 3mpi and 6mpi**

186 The PhNR of the SOHU eyes decreased at all time points after SO injection, but only reached
187 statistical significance at 1mpi (**Fig. 8A**). The *in vivo* OCT imaging of the retinas detected edema
188 (thickening) of RNFL in the SOHU eyes at 3mpi and significant thinning at 6mpi (**Fig. 8B**),
189 indicating inner retina neurodegeneration. Post-mortem histological analysis confirmed the
190 significant RGC and ON degeneration at both 3mpi and 6mpi (**Fig. 9**).

Discussion

A reliable NHP glaucoma model that closely mimics the disease in humans is a prerequisite for studies of pathogenetic mechanisms and for selecting efficient neuroprotective treatments for clinical use. In the present study, we demonstrated that SO intracameral injection induces glaucomatous neurodegeneration in rhesus macaque monkey eyes, that replicates both the mouse SOHU glaucoma model and human secondary glaucoma. After a simple SO intracameral injection procedure, all the SOHU eyes showed significant thinning of RNFL, decreased visual function (PhNR), and loss of RGC somata and axons within 3-6 months. The reversible intracameral SO injection does not cause overt ocular structural damage while simulating acute glaucomatous changes. Therefore, this relatively acute and severe glaucomatous neurodegeneration of this SOHU NHP model can be used to model angle-closure glaucoma, which is responsible for 50% of blindness caused by glaucoma (Pohl and Tarnutzer, 2018; Tham et al., 2014). In addition to its usefulness to decipher the molecular mechanisms of ocular hypertension-induced glaucomatous degeneration in primate, this inducible and clinically relevant NHP neurodegeneration model will be valuable to preclinically assess the efficacy and safety of experimental neuroprotection and regeneration therapies.

It also notable that the characteristic human glaucoma features associated with the most extensively studied animal (#38361), including stable, lasting, and reversible ocular hypertension, ONH “cupping”, quadrant specific RNFL thinning, PhNR deficits, and dramatic RGC/ON degeneration, suggest that this model has the potential to replicate chronic glaucoma in human patients. Unfortunately, most animals we tested did not react in the same way as this one. On the contrary, they showed low IOP in the SOHU eyes at some points. We observed rapid IOP elevation

214 immediately after SO injection in some but not all the animals before they developed severe ocular
215 hypotension. We suspect that the pupillary blockade substantially elevated the IOP in a very short
216 period of time and that caused ciliary body "shutdown" happened in human patients (Coleman,
217 1995). In this case, the ciliary body stops generating aqueous humor, which leads to ocular
218 hypotension. Consistent with acute IOP elevation resulting in ischemic changes, we observed fixed
219 dilated pupils in all SOHU eyes that was likely due to iris ischemia. For reasons that we do not
220 understand at this point, some animals, such as #38361, can recover rather quickly from ciliary
221 body shock and resume aqueous humor production, which increases IOP due to pupillary blocking.
222 However, other animals may not be able to recover from ciliary body shock to maintain normal
223 IOP, such as animals #44876 and #45513. In some animals IOP slowly returned to normal, such
224 as animals #42946, #44639, #44193, indicating partial ciliary body recovery. We hypothesize that
225 either the ciliary body is not fully recovered so that it cannot further elevate IOP even when
226 pupillary blocking by SO is still in place, or the eye may need more time to finally achieve ocular
227 hypertension. We do not know what causes the different responses of different animals at this
228 point. Age may play a role since #38361 was much older (13yrs) than the other five animals (6-
229 8yrs). Further systematic studies with additional NHP animals are needed to clarify the reasons
230 and to further optimize this model. For example, a modified SOHU model that induces and
231 maintains a moderate elevation of IOP through frequent pupil dilation (Fang et al., 2021) may
232 prevent the acute very high IOP elevation causing ciliary body shock.
233
234 Ocular vascular dysfunction has long been known to be correlated with the incidence of glaucoma
235 and acute high IOP elevation in patients with angle-closure glaucoma, and secondary glaucoma
236 can induce central retinal artery occlusion with ischemic damage of the inner retina (Flammer et

237 al., 2002; Mozaffarieh et al., 2008; Osborne et al., 2004; Wareham and Calkins, 2020). We
238 previously detected ocular ischemia with inner retina damage and outer retina sparing in the severe
239 variant of the SOHU mouse model (Fang et al., 2021), consistent with findings in rats with acute
240 high IOP elevation (Buchi et al., 1991; Chidlow et al., 2010; Hughes, 1991; Smith and Baird,
241 1952). Interestingly, we also detected ocular branch artery occlusion in the animal (#38361) with
242 high IOP elevation, demonstrating another similarity of the SOHU NHP model to the human acute
243 glaucoma-related syndrome.
244
245 Despite the absence of long-lasting ocular hypertension, the five other animals all showed RGC
246 and ON degeneration. This suggests that transient acute IOP elevation causes the
247 neurodegeneration. From our mouse study (Fang et al., 2021), we learned that although SO
248 removal allows IOP to return quickly to normal, it does not stop the progression of glaucomatous
249 neurodegeneration in the SOHU model. This result is also consistent with the clinical observation
250 that visual field loss can progress aggressively in some glaucoma patients whose IOP is maintained
251 at a relatively low level. Thus, this NHP SOHU model can be used to determine the efficacy of
252 experimental neuroprotection treatment under a low IOP condition after initial pathogenic ocular
253 hypertension. Advanced retinal imaging and visual function assays that are available for humans
254 can be applied to this primate glaucoma model. These assays will identify morphological and
255 functional changes in RGCs and ON that can serve as potential biomarkers in glaucoma and other
256 optic neuropathies. Since optic neuropathy can also be associated with other central nervous
257 system (CNS) neurodegenerative diseases (Carelli et al., 2017), including multiple sclerosis
258 (Balcer et al., 2015; Talman et al., 2010; Toosy et al., 2014), Alzheimer's disease (Chiasseu et al.,

259 2016; McKinnon, 2003), and amyotrophic lateral sclerosis (Minegishi et al., 2016; Wiggs and
260 Pasquale, 2017), this model may be broadly applicable to diverse CNS degenerative diseases.

261

262

263

Acknowledgements

We thank Drs. Jeffrey Goldberg, Jie Zhang, Xin Duan, Derek Welsbie, Anna La Torre Vila, and Alan Tessler for critical discussion and reading the manuscript. Y.H. is supported by CNPRC Pilot Grant, NIH grants EY031063, EY024932, EY023295, EY028106, and EY032518, and grants from Glaucoma Research Foundation (CFC3), BrightFocus Foundation, Chan Zuckerberg Initiative Neurodegeneration Collaborative Pairs Pilot Projects, Stanford SPARK program and Stanford Center for Optic Disc Drusen. We are grateful for an unrestricted grant from Research to Prevent Blindness and NEI P30 EY026877 to the Department of Ophthalmology, Stanford University.

Author contributions: Y.H., A.M., and F.F. designed the experiments. A.M. performed surgeries and eye exams, F.F., P.Z., H.H., X.F., L.L., and R.D. processed the samples. Y.H., F.F., and A.M. analyzed the data and prepared the manuscript.

Competing interests

YH is a consultant for Janssen BioPharma, Inc.

A patent application has been submitted by Stanford Office of Technology Licensing for SOHU animal glaucoma model that is related to this manuscript.

The authors have declared that no conflict of interest exists.

285 **Materials and Methods**

286 **Animals**. The animals in this study were rhesus macaques (Macaca mulatta) born and maintained
287 at the California National Primate Research Center (CNPRC). The CNPRC is accredited by the
288 Association for Assessment and Accreditation of Laboratory Animal Care (AAALAC)
289 International. Guidelines of the Association for Research in Vision and Ophthalmology Statement
290 for the Use of Animals in Ophthalmic and Vision Research were followed. All aspects of this study
291 were in accordance with the National Institutes of Health (NIH) Guide for the Care and Use of
292 Laboratory Animals. Phenotyping and ophthalmic examinations were performed according to an
293 animal protocol approved by the University of California Davis Institutional Animal Care and Use
294 Committee and Stanford University School of Medicine.

295

296 **Intracameral injection of SO**. The procedure is similar to the published protocol (Zhang et al.,
297 2019a; Zhang et al., 2019b) but with modification for monkey eyes. Sedation was achieved by
298 intramuscular injection of ketamine hydrochloride (5-30 mg/kg IM) and dexmedetomidine (0.05-
299 0.075 mg/kg IM). The eyes were prepped in a usual sterile fashion for ophthalmic surgery
300 including topical anesthetic 0.5% proparacaine hydrochloride (Akorn, Somerset, New Jersey)
301 followed by 5% betadine to the ocular surface and adnexa. A disposable 15-degree blade was used
302 to make a side-port incision at the corneal limbus to enter the anterior chamber inferiorly near the
303 6 o'clock position in order to minimize the likelihood of oil leaking out of the eye. Silicone oil
304 (SO, 1,000 mPa.s, Silikon, Alcon Laboratories, Fort Worth, Texas) in a 3 cc syringe on a bent 25
305 gauge cannula was introduced into the anterior chamber. SO was injected little by little, stopping
306 intermittently with gentle pressure applied to the posterior aspect of the limbal incision to allow
307 for aqueous humor to exit the eye. Oil was injected to fill the anterior chamber to a physiologic

308 depth with roughly ~70-80% silicone oil and to cover the entire pupil with ~ 100 µl volume. After
309 the injection, the wound was tested to insure it was self-sealing and veterinary antibiotic ointment
310 (BNP Ophthalmic Ointment, Vetropolycin, Dechra, Overland Park, Kansas) was applied to the
311 surface of the injected eye. The contralateral control eyes received a mock injection with no
312 penetration of the eye. Animals were monitored by a trained technician and a veterinarian at all
313 times.
314
315 **Removing SO from the anterior chamber.** The procedure is similar to the published protocol
316 (Zhang et al., 2019a; Zhang et al., 2019b) with modification for monkey eyes. Briefly, after the
317 animal was anesthetized the eye was prepped in a sterile fashion as above. A superior (12 o'clock)
318 corneal side-port incision was made using a 15-degree blade at the corneal limbus. A 3 cc syringe
319 filled with sterile balanced salt solution (BSS Plus, Alcon Laboratories, Ft. Worth, Texas) with a
320 25 gauge bent cannula was introduced into the anterior chamber and saline was gently injected
321 little by little while periodically allowing oil to egress from the same incision by gently applying
322 pressure to the posterior aspect of the wound. After removing all of the oil and replacing it
323 incrementally with BSS to a physiologic depth, the cannula was removed and the wound was
324 checked to be self-sealing, after which antibiotic ointment was applied.
325
326 **Eye examinations and retinal fundus imaging.** Sedated ophthalmic examination included
327 measurement of intraocular pressure (IOP) using rebound tonometry (Icare TA01i, Finland) while
328 the animal was held upright and with careful attention not to apply any pressure to the globe. Three
329 IOP measurements were taken and averaged at each exam date. Examination also included
330 pupillary light reflex testing, external and portable slit lamp examination, as well as dilated

331 (Tropicamide 1%, Phenylephrine 2.5%, Cyclopentolate 1%) indirect ophthalmoscopy. Sedation
332 was achieved by intramuscular injection of ketamine hydrochloride (5-30 mg/kg IM) and
333 dexmedetomidine (0.05-0.075 mg/kg IM). Animals were monitored by a trained technician and a
334 veterinarian at all times. Color and red-free fundus photographs were obtained with the CF-1
335 Retinal Camera with a 50˚ wide angle lens (Canon, Tokyo, Japan).
336
337 **Spectral-domain optical coherence tomography (SD-OCT) imaging.** SD-OCT with confocal
338 scanning laser ophthalmoscopy (cSLO) was also performed (Spectralis® HRA+OCT, Heidelberg,
339 Germany). High-resolution radial and circumferential scans centered on the optic nerve were
340 obtained using a corneal curvature (K) value of 6.5 mm radius. For the high-resolution radial scans
341 of the optic nerve head (ONH), 48 radial B-scans were acquired by 870 nm SD-OCT (Spectralis;
342 Heidelberg Engineering, GmbH), over a 30° area, and 768 A-scans per B-scan at ART=16
343 repetitions. All repetitive scans were acquired using eye-tracking and averaged to reduce speckle
344 noise. We read in all the images and measured MRW, RimV, and CupV using R program. The
345 codes that we used to calculate MRW, RimV and CupV are at Github (https://github.com/HuLab-
346 Code/ONHV). For each monkey eye, the center of the ONH was estimated and registered during
347 the first imaging session and used to align all follow-up images. All imaging was done by the
348 same ophthalmic imaging team. All OCT images were taken through the center of the pupil.
349 Speculums were used and corneal hydration was maintained through application of topical
350 lubrication (Genteal artificial tears) approximately every 1-2 minutes during imaging sessions.
351 The en-face retinal images were captured with the Heidelberg Spectralis SLO/OCT system
352 equipped with an 870nm infrared wavelength light source and a 30º lens (Heidelberg
353 Engineering). The average thickness of retinal nerve fiber layer (RNFL) around the optic nerve

head was measured manually with the aid of Heidelberg software. The investigators who measured the thickness of RNFL were masked to the treatment of the samples.

Electroretinogram (ERG) recording. After dilation, a full-field ERG (ffERG) containing six different tests was performed on each eye following a 30-minute dark adaptation period. ERG-Jet electrodes (item #95-011) were coupled with the RETeval instrument (LKC Technologies, Gaithersburg, MD, United States), as previously described (Lin et al., 2021). A standard flash electroretinogram was performed according to the approved protocol of the International Society for Clinical Electrophysiology of Vision (ISCEV). There were four dark adapted tests (0.01 cd*s/m2, 3.0 cd*s/m2, 10.0 cd*s/m2, and oscillatory potentials 3.0 cd*s/m2). After 10 minutes of light adaptation, two additional tests were performed (3.0 cd*s/m2 single flash with measurement of the photopic negative response and photopic flicker 3.0 cd*s/m2). Both time (ms) and amplitude (μV) were obtained for each test on each eye. Single flash tests measured an a-wave and b-wave. Oscillatory potentials measured five wave points and a sum. In the photopic flicker test, the first wave point is reported. Measurements were recorded and displayed using the manufacturer's software.

Immunohistochemistry of whole-mount retina and RGC counting. The detailed procedure has been published before (Li et al., 2020; Zhang et al., 2019a; Zhang et al., 2019b) with modification to accommodate large monkey eyes. Briefly, after intravitreal injection with 10% formalin in PBS, the eyes and optic nerves were dissected out, post-fixed with 10% formalin for 24 hours at room temperature. Retinas were dissected out and washed extensively in PBS before blocking in staining buffer (10% normal goat serum, Sigma-Aldrich, and 2% Triton X-100 in PBS) for half an hour.

377 RBPMS guinea pig antibody made at ProSci Inc (Poway, California) according to publications
378 (Kwong et al., 2010; Rodriguez et al., 2014) was diluted (1:4000) in the same staining buffer.
379 Floating retinas were incubated with primary antibodies overnight at 4°C and washed 3 times for
380 30 minutes each with PBS. Secondary antibodies (Cy3) were then applied (1:200; Jackson
381 ImmunoResearch, West Grove, Pennsylvania) and incubated for 1 hour at room temperature.
382 Retinas were again washed 3 times for 30 minutes each with PBS before a cover slip was attached
383 with Fluoromount-G (SouthernBiotech, Birmingham, Alabama). For RGC counting, whole-mount
384 retinas were immunostained with the RBPMS antibody, 6 fields sampled from each region
385 (periphery, mid-periphery, and center retinas) using a 20x lens with Keyence epifluorescence
386 microscope, and $RBPMS^+$ RGCs of each image (540 µm x 720 µm) were counted manually with
387 Fiji/ImageJ. The investigators who counted the cells were masked to the treatment of the samples.
388

389 **ON semi-thin sections and quantification of surviving axons.** The detailed procedure has been
390 published before (Li et al., 2020; Zhang et al., 2019a; Zhang et al., 2019b). Briefly, the ON was
391 exposed by removing the brain and post-fixed *in situ* using 2% glutaraldehyde/ 2% PFA in 0.1M
392 PB for 4 hours on ice. Samples were then washed with 0.1M PB 3 times, 10 minutes each wash.
393 The ONs were then carefully dissected out and rinsed with 0.1M PB 3 times, 10 minutes each
394 wash. They were then incubated in 1% osmium tetroxide in 0.1M PB for 1 hour at room
395 temperature followed by washing with 0.1M PB for 10 minutes and water for 5 minutes. ONs were
396 next dehydrated through graded ethanol, infiltrated in propylene oxide and epoxy, and embedded
397 in epoxy at 60°C for 24 hours. Semi-thin sections (1 µm) were cut on an ultramicrotome (EM
398 UC7, Leica) and collected 2 mm distal to the eye. The semi-thin sections were attached to glass
399 slides and stained with 1% para-phenylenediamine (PPD) in methanol: isopropanol (1:1) for 35

400 minutes. After rinsing 3 times with methanol: isopropanol (1:1), coverslips were applied with
401 Permount Mounting Medium (Electron Microscopy Sciences, Hatfield, Pennsylvania). PPD stains
402 all myelin sheaths, but darkly stains the axoplasm only of degenerating axons, which allows us to
403 differentiate surviving axons from degenerating axons (Smith, 2002). The whole ON were imaged
404 with a 100x lens of a Keyence fluorescence microscopy to cover the entire area of the ON without
405 overlap. Four areas of 108 µm x 144 µm were cropped, and the surviving axons within the
406 designated areas counted manually with Fiji/ImageJ. After counting all the images taken from a
407 single nerve, the mean of the surviving axon number was calculated for each ON. The investigators
408 who counted the axons were masked to the treatment of the samples.
409
410 **Retina cross sections and H&E and Trichrome Staining.** Monkey eyes were enucleated and
411 immediately fixed in 10% formalin for 36 hours at room temperature. They were processed
412 through graded alcohol and xylene, then infiltrated and embedded in paraffin. Six-micron sections
413 were taken and stained with Hematoxylin & Eosin (H&E) to look at the cell nuclei, extracellular
414 matrix, and cytoplasm. Standard protocol was followed to stain these slides. The Trichrome kit
415 was purchased from Abcam (ab 150686) to study collagenous connective tissue in sections. Slides
416 were deparaffinized and incubated in preheated Bouin's fluid for an hour and rinsed in water. They
417 were then incubated in Weigert's Iron Hematoxylin for 5 minutes, rinsed in water again and then
418 incubated in Biebrich Scarlet/Acid Fuchsin solution for 15 minutes. They were rinsed in water
419 again. Sections were then differentiated in phosphotungstic acid solution for 10-15 minutes (or
420 until collagen is not red), incubated in Aniline Blue solution for 5-10 minutes and rinsed in water.
421 Acetic acid solution was applied to these sections for 3-5 minutes, and slides were then dehydrated
422 in alcohol, cleared in xylene, and mounted with CytoSeal 60 (from Electron Microscopy Sciences,

423 18006). This stain shows a stronger collagen stain (blue green stain) in glaucomatous eye than the
424 control eye.
425
426 **Statistical analyses.** GraphPad Prism 7 was used to generate graphs and for statistical analyses.
427 Data are presented as means ± s.e.m. Student's t-test was used for two groups comparison and
428 One-way ANOVA with post hoc test was used for multiple comparisons.

429 **References**

430

431

432 Aktas, O., P. Albrecht, and H.P. Hartung. 2016. Optic neuritis as a phase 2 paradigm for neuroprotection therapies
433 of multiple sclerosis: update on current trials and perspectives. *Current opinion in neurology* 29:199-204.
434 Anderson, D.R., and S. Normal Tension Glaucoma. 2003. Collaborative normal tension glaucoma study. *Curr Opin*
435 *Ophthalmol* 14:86-90.
436 Balcer, L.J., D.H. Miller, S.C. Reingold, and J.A. Cohen. 2015. Vision and vision-related outcome measures in
437 multiple sclerosis. *Brain* 138:11-27.
438 Beykin, G., A.M. Norcia, V.J. Srinivasan, A. Dubra, and J.L. Goldberg. 2021. Discovery and clinical translation of
439 novel glaucoma biomarkers. *Prog Retin Eye Res* 80:100875.
440 Buchi, E.R., I. Suivaizdis, and J. Fu. 1991. Pressure-induced retinal ischemia in rats: an experimental model for
441 quantitative study. *Ophthalmologica* 203:138-147.
442 Burgoyne, C. 2015a. The morphological difference between glaucoma and other optic neuropathies. *Journal of*
443 *neuro-ophthalmology : the official journal of the North American Neuro-Ophthalmology Society* 35 Suppl
444 1:S8-S21.
445 Burgoyne, C.F. 2011. A biomechanical paradigm for axonal insult within the optic nerve head in aging and
446 glaucoma. *Experimental eye research* 93:120-132.
447 Burgoyne, C.F. 2015b. The non-human primate experimental glaucoma model. *Experimental eye research* 141:57-
448 73.
449 Calkins, D.J. 2012. Critical pathogenic events underlying progression of neurodegeneration in glaucoma. *Prog Retin*
450 *Eye Res* 31:702-719.
451 Calkins, D.J. 2021. Adaptive responses to neurodegenerative stress in glaucoma. *Prog Retin Eye Res* 100953.
452 Carelli, V., C. La Morgia, F.N. Ross-Cisneros, and A.A. Sadun. 2017. Optic neuropathies: the tip of the
453 neurodegeneration iceberg. *Hum Mol Genet* 26:R139-R150.
454 Chen, L., Y. Zhao, and H. Zhang. 2016. Comparative Anatomy of the Trabecular Meshwork, the Optic Nerve Head
455 and the Inner Retina in Rodent and Primate Models Used for Glaucoma Research. *Vision (Basel)* 1:
456 Chiasseu, M., J.L. Cueva Vargas, L. Destroismaisons, C. Vande Velde, N. Leclerc, and A. Di Polo. 2016. Tau
457 Accumulation, Altered Phosphorylation, and Missorting Promote Neurodegeneration in Glaucoma. *J*
458 *Neurosci* 36:5785-5798.
459 Chidlow, G., M.C. Holman, J.P. Wood, and R.J. Casson. 2010. Spatiotemporal characterization of optic nerve
460 degeneration after chronic hypoperfusion in the rat. *Invest Ophthalmol Vis Sci* 51:1483-1497.
461 Coleman, D.J. 1995. Evaluation of ciliary body detachment in hypotony. *Retina* 15:312-318.
462 Costello, F., S. Coupland, W. Hodge, G.R. Lorello, J. Koroluk, Y.I. Pan, M.S. Freedman, D.H. Zackon, and R.H.
463 Kardon. 2006. Quantifying axonal loss after optic neuritis with optical coherence tomography. *Annals of*
464 *neurology* 59:963-969.
465 Downs, J.C., and C.A. Girkin. 2017. Lamina cribrosa in glaucoma. *Curr Opin Ophthalmol* 28:113-119.
466 Fang, F., J. Zhang, P. Zhuang, P. Liu, L. Li, H. Huang, H.C. Webber, Y. Xu, L. Liu, R. Dalal, Y. Sun, and Y. Hu.
467 2021. Chronic mild and acute severe glaucomatous neurodegeneration derived from silicone oil-induced
468 ocular hypertension. *Scientific reports* 11:9052.
469 Flammer, J., S. Orgul, V.P. Costa, N. Orzalesi, G.K. Krieglstein, L.M. Serra, J.P. Renard, and E. Stefansson. 2002.
470 The impact of ocular blood flow in glaucoma. *Prog Retin Eye Res* 21:359-393.
471 Flores-Sanchez, B.C., and A.J. Tatham. 2019. Acute angle closure glaucoma. *Br J Hosp Med (Lond)* 80:C174-C179.
472 Garway-Heath, D.F., D.P. Crabb, C. Bunce, G. Lascaratos, F. Amalfitano, N. Anand, A. Azuara-Blanco, R.R.
473 Bourne, D.C. Broadway, I.A. Cunliffe, J.P. Diamond, S.G. Fraser, T.A. Ho, K.R. Martin, A.I. McNaught,
474 A. Negi, K. Patel, R.A. Russell, A. Shah, P.G. Spry, K. Suzuki, E.T. White, R.P. Wormald, W. Xing, and
475 T.G. Zeyen. 2015. Latanoprost for open-angle glaucoma (UKGTS): a randomised, multicentre, placebo-
476 controlled trial. *Lancet* 385:1295-1304.
477 Harwerth, R.S., and E.L. Smith, 3rd. 1985. Rhesus monkey as a model for normal vision of humans. *Am J Optom*
478 *Physiol Opt* 62:633-641.
479 He, L., H. Yang, S.K. Gardiner, G. Williams, C. Hardin, N.G. Strouthidis, B. Fortune, and C.F. Burgoyne. 2014.
480 Longitudinal detection of optic nerve head changes by spectral domain optical coherence tomography in
481 early experimental glaucoma. *Invest Ophthalmol Vis Sci* 55:574-586.

482 Heijl, A., M.C. Leske, B. Bengtsson, L. Hyman, B. Bengtsson, M. Hussein, and G. Early Manifest Glaucoma Trial.
483 2002. Reduction of intraocular pressure and glaucoma progression: results from the Early Manifest
484 Glaucoma Trial. *Arch Ophthalmol* 120:1268-1279.
485 Hopkins, A.A., R. Murphy, M. Irnaten, D.M. Wallace, B. Quill, and C. O'Brien. 2020. The role of lamina cribrosa
486 tissue stiffness and fibrosis as fundamental biomechanical drivers of pathological glaucoma cupping. *Am J*
487 *Physiol Cell Physiol* 319:C611-C623.
488 Howell, G.R., R.T. Libby, T.C. Jakobs, R.S. Smith, F.C. Phalan, J.W. Barter, J.M. Barbay, J.K. Marchant, N.
489 Mahesh, V. Porciatti, A.V. Whitmore, R.H. Masland, and S.W. John. 2007. Axons of retinal ganglion cells
490 are insulted in the optic nerve early in DBA/2J glaucoma. *J Cell Biol* 179:1523-1537.
491 Hughes, W.F. 1991. Quantitation of ischemic damage in the rat retina. *Experimental eye research* 53:573-582.
492 Ichhpujani, P., A. Jindal, and L. Jay Katz. 2009. Silicone oil induced glaucoma: a review. *Graefe's archive for*
493 *clinical and experimental ophthalmology = Albrecht von Graefes Archiv fur klinische und experimentelle*
494 *Ophthalmologie* 247:1585-1593.
495 Iyer, J., J.R. Vianna, B.C. Chauhan, and H.A. Quigley. 2020. Toward a new definition of glaucomatous optic
496 neuropathy for clinical research. *Curr Opin Ophthalmol* 31:85-90.
497 Kim, J.A., T.W. Kim, R.N. Weinreb, E.J. Lee, M.J.A. Girard, and J.M. Mari. 2018. Lamina Cribrosa Morphology
498 Predicts Progressive Retinal Nerve Fiber Layer Loss In Eyes with Suspected Glaucoma. *Scientific reports*
499 8:738.
500 Kornmann, H.L., and S.J. Gedde. 2016. Glaucoma management after vitreoretinal surgeries. *Curr Opin Ophthalmol*
501 27:125-131.
502 Kwong, J.M., J. Caprioli, and N. Piri. 2010. RNA binding protein with multiple splicing: a new marker for retinal
503 ganglion cells. *Invest Ophthalmol Vis Sci* 51:1052-1058.
504 Li, L., H. Huang, F. Fang, L. Liu, Y. Sun, and Y. Hu. 2020. Longitudinal Morphological and Functional Assessment
505 of RGC Neurodegeneration After Optic Nerve Crush in Mouse. *Frontiers in cellular neuroscience* 14:109.
506 Lin, K.H., T. Tran, S. Kim, S. Park, J.T. Stout, R. Chen, J. Rogers, G. Yiu, S. Thomasy, and A. Moshiri. 2021.
507 Advanced Retinal Imaging and Ocular Parameters of the Rhesus Macaque Eye. *Translational vision*
508 *science & technology* 10:7.
509 Lockwood, H., J. Reynaud, S. Gardiner, J. Grimm, V. Libertiaux, J.C. Downs, H. Yang, and C.F. Burgoyne. 2015.
510 Lamina cribrosa microarchitecture in normal monkey eyes part 1: methods and initial results. *Invest*
511 *Ophthalmol Vis Sci* 56:1618-1637.
512 Maupin, E., F. Baudin, L. Arnould, A. Seydou, C. Binquet, A.M. Bron, and C.P. Creuzot-Garcher. 2020. Accuracy
513 of the ISNT rule and its variants for differentiating glaucomatous from normal eyes in a population-based
514 study. *The British journal of ophthalmology* 104:1412-1417.
515 McKinnon, S.J. 2003. Glaucoma: ocular Alzheimer's disease? *Front Biosci* 8:s1140-1156.
516 Minegishi, Y., M. Nakayama, D. Iejima, K. Kawase, and T. Iwata. 2016. Significance of optineurin mutations in
517 glaucoma and other diseases. *Prog Retin Eye Res* 55:149-181.
518 Mozaffarieh, M., M.C. Grieshaber, and J. Flammer. 2008. Oxygen and blood flow: players in the pathogenesis of
519 glaucoma. *Mol Vis* 14:224-233.
520 Osborne, N.N., R.J. Casson, J.P. Wood, G. Chidlow, M. Graham, and J. Melena. 2004. Retinal ischemia:
521 mechanisms of damage and potential therapeutic strategies. *Prog Retin Eye Res* 23:91-147.
522 Pohl, H., and A.A. Tarnutzer. 2018. Acute Angle-Closure Glaucoma. *N Engl J Med* 378:e14.
523 Rodriguez, A.R., L.P. de Sevilla Muller, and N.C. Brecha. 2014. The RNA binding protein RBPMS is a selective
524 marker of ganglion cells in the mammalian retina. *The Journal of comparative neurology* 522:1411-1443.
525 Smith, G.G., and C.D. Baird. 1952. Survival time of retinal cells when deprived of their blood supply by increased
526 intraocular pressure. *American journal of ophthalmology* 35:133-136.
527 Smith, R.S. 2002. Systematic evaluation of the mouse eye : anatomy, pathology, and biomethods. CRC Press, Boca
528 Raton. 366 p. pp.
529 Talman, L.S., E.R. Bisker, D.J. Sackel, D.A. Long, Jr., K.M. Galetta, J.N. Ratchford, D.J. Lile, S.K. Farrell, M.J.
530 Loguidice, G. Remington, A. Conger, T.C. Frohman, D.A. Jacobs, C.E. Markowitz, G.R. Cutter, G.S.
531 Ying, Y. Dai, M.G. Maguire, S.L. Galetta, E.M. Frohman, P.A. Calabresi, and L.J. Balcer. 2010.
532 Longitudinal study of vision and retinal nerve fiber layer thickness in multiple sclerosis. *Annals of*
533 *neurology* 67:749-760.
534 Tham, Y.C., X. Li, T.Y. Wong, H.A. Quigley, T. Aung, and C.Y. Cheng. 2014. Global prevalence of glaucoma and
535 projections of glaucoma burden through 2040: a systematic review and meta-analysis. *Ophthalmology*
536 121:2081-2090.
537 Toosy, A.T., D.F. Mason, and D.H. Miller. 2014. Optic neuritis. *Lancet neurology* 13:83-99.

538 Varma, D.D., S. Cugati, A.W. Lee, and C.S. Chen. 2013. A review of central retinal artery occlusion: clinical
539 presentation and management. *Eye (Lond)* 27:688-697.
540 Viswanathan, S., L.J. Frishman, J.G. Robson, R.S. Harwerth, and E.L. Smith, 3rd. 1999. The photopic negative
541 response of the macaque electroretinogram: reduction by experimental glaucoma. *Invest Ophthalmol Vis*
542 *Sci* 40:1124-1136.
543 Wareham, L.K., and D.J. Calkins. 2020. The Neurovascular Unit in Glaucomatous Neurodegeneration. *Front Cell*
544 *Dev Biol* 8:452.
545 Wareham, L.K., M.L. Risner, and D.J. Calkins. 2020. Protect, Repair, and Regenerate: Towards Restoring Vision in
546 Glaucoma. *Curr Ophthalmol Rep* 8:301-310.
547 Weinreb, R.N., C.K. Leung, J.G. Crowston, F.A. Medeiros, D.S. Friedman, J.L. Wiggs, and K.R. Martin. 2016.
548 Primary open-angle glaucoma. *Nat Rev Dis Primers* 2:16067.
549 Wiggs, J.L., and L.R. Pasquale. 2017. Genetics of glaucoma. *Hum Mol Genet* 26:R21-R27.
550 Wilsey, L., S. Gowrisankaran, G. Cull, C. Hardin, C.F. Burgoyne, and B. Fortune. 2017. Comparing three different
551 modes of electroretinography in experimental glaucoma: diagnostic performance and correlation to
552 structure. *Documenta ophthalmologica. Advances in ophthalmology* 134:111-128.
553 Wormald, R., G. Virgili, and A. Azuara-Blanco. 2020. Systematic reviews and randomised controlled trials on open
554 angle glaucoma. *Eye (Lond)* 34:161-167.
555 Yang, H., J. Reynaud, H. Lockwood, G. Williams, C. Hardin, L. Reyes, C. Stowell, S.K. Gardiner, and C.F.
556 Burgoyne. 2017. The connective tissue phenotype of glaucomatous cupping in the monkey eye - Clinical
557 and research implications. *Prog Retin Eye Res* 59:1-52.
558 Zhang, J., F. Fang, L. Li, H. Huang, H.C. Webber, Y. Sun, V.B. Mahajan, and Y. Hu. 2019a. A Reversible Silicon
559 Oil-Induced Ocular Hypertension Model in Mice. *Journal of visualized experiments : JoVE* 153:
560 Zhang, J., L. Li, H. Huang, F. Fang, H.C. Webber, P. Zhuang, L. Liu, R. Dalal, P.H. Tang, V.B. Mahajan, Y. Sun, S.
561 Li, M. Zhang, J.L. Goldberg, and Y. Hu. 2019b. Silicone oil-induced ocular hypertension and
562 glaucomatous neurodegeneration in mouse. *eLife* 8:
563
564

565 **Figure Legends**

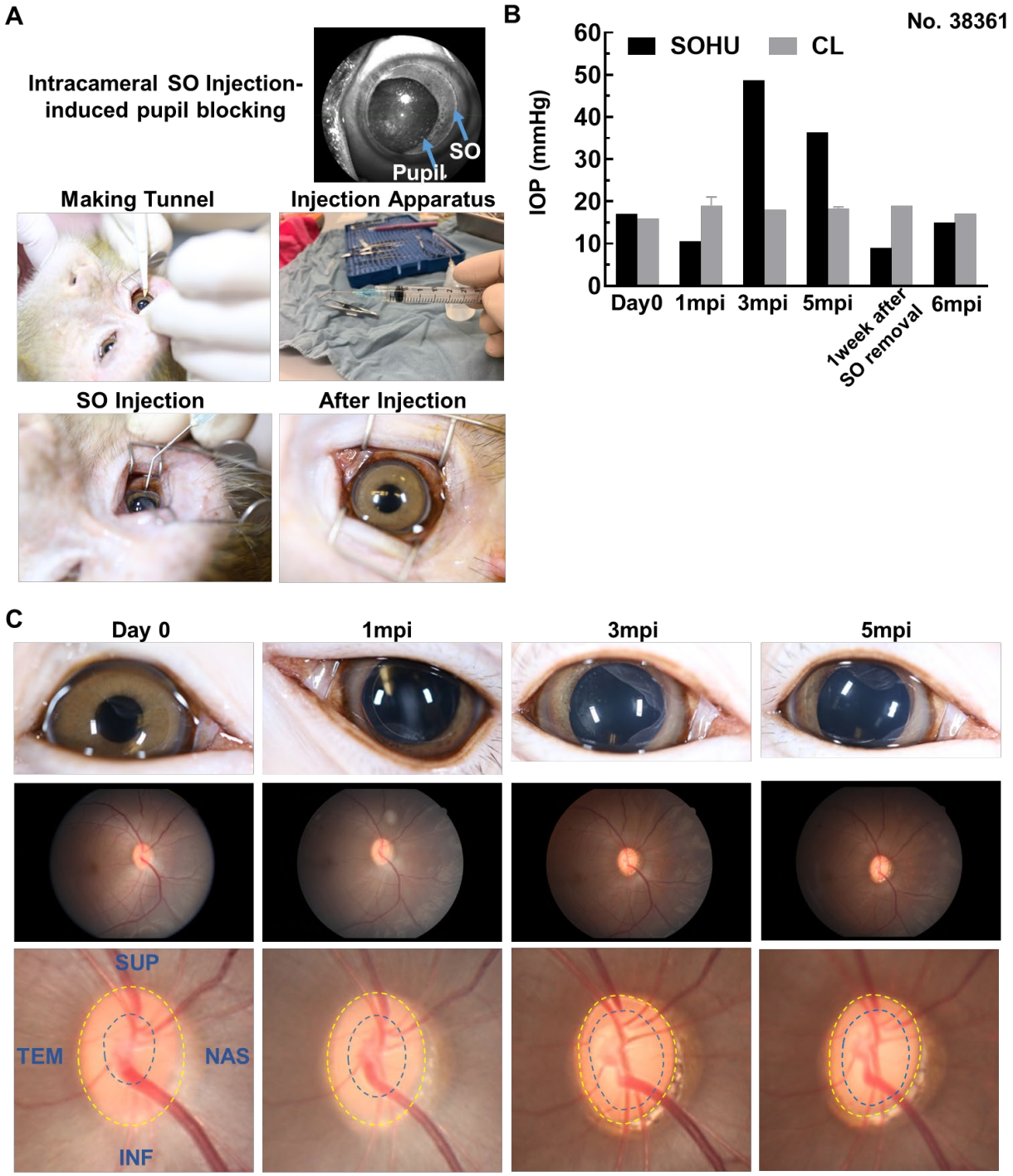

566

567 **Figure 1. Intracameral SO injection-induced IOP elevation and ONH "cupping" in animal**

568 **#38361.** (**A**) The procedures of SO intracameral injection in monkey eye. (**B**) Longitudinal IOP

measurements of experimental (SOHU) eye and contralateral control (CL) eyes at different time points after SO injection. mpi: month post injection. (**C**) The retinal fundus images of the SOHU eye before and after SO injection. Yellow dotted line outlines the optic disc; blue dotted line outlines optic cup.

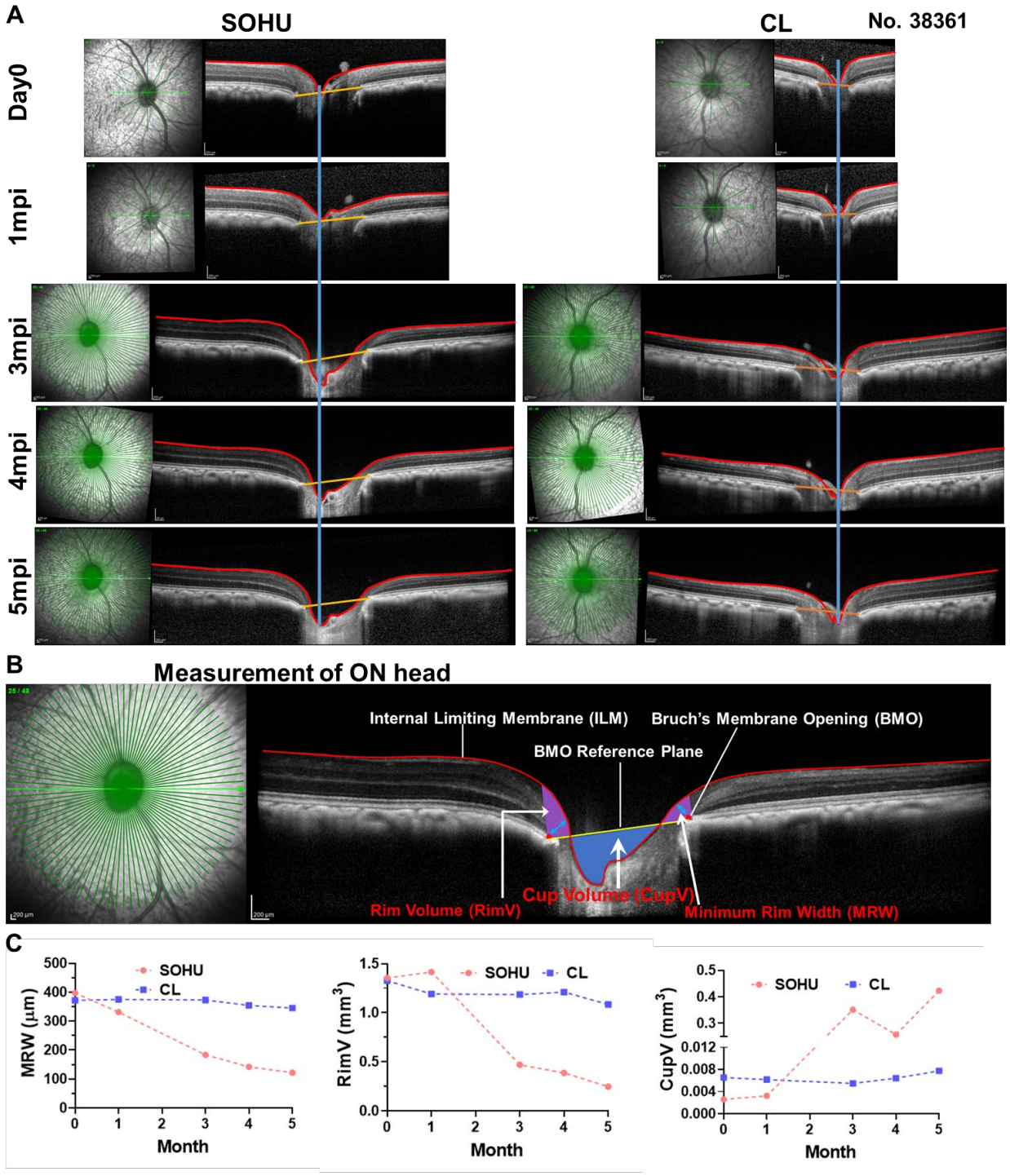

576

577

578 **Figure 2. Delineated live OCT images of ONH and measurements in SOHU and CL eyes of**

579 **animal #38361.** (**A**) Longitudinal SD-OCT imaging of macaque ON head with 48 radial B-scans

580 acquired over a 30° area at 768 A-scans per B-scan, ART=16 repetitions. (**B**) Neural tissue
581 parameters: Minimum rim width (MRW, blue double headed arrow) was measured at each
582 delineated Bruch's membrane opening point (BMO, red dot) as the minimum distance to ILM;
583 Rim volume (RimV, purple area) was calculated from the volume bounded by ILM (red line),
584 BMO reference plane (yellow line) and perpendicular line through the BMO; Cup volume (CupV,
585 blue area) was generated from the volume between ILM surface and the BMO reference plane.
586 (**C**) The raw OCT images were transformed to the gray value matrix. The noise from the image
587 acquisition and transformation was reduced by Gaussian filter. After the denoise processing, then
588 3D model and the MRW, RimV and CupV were established by Otsu's thresholding method and
589 convolutional neural network method.
590

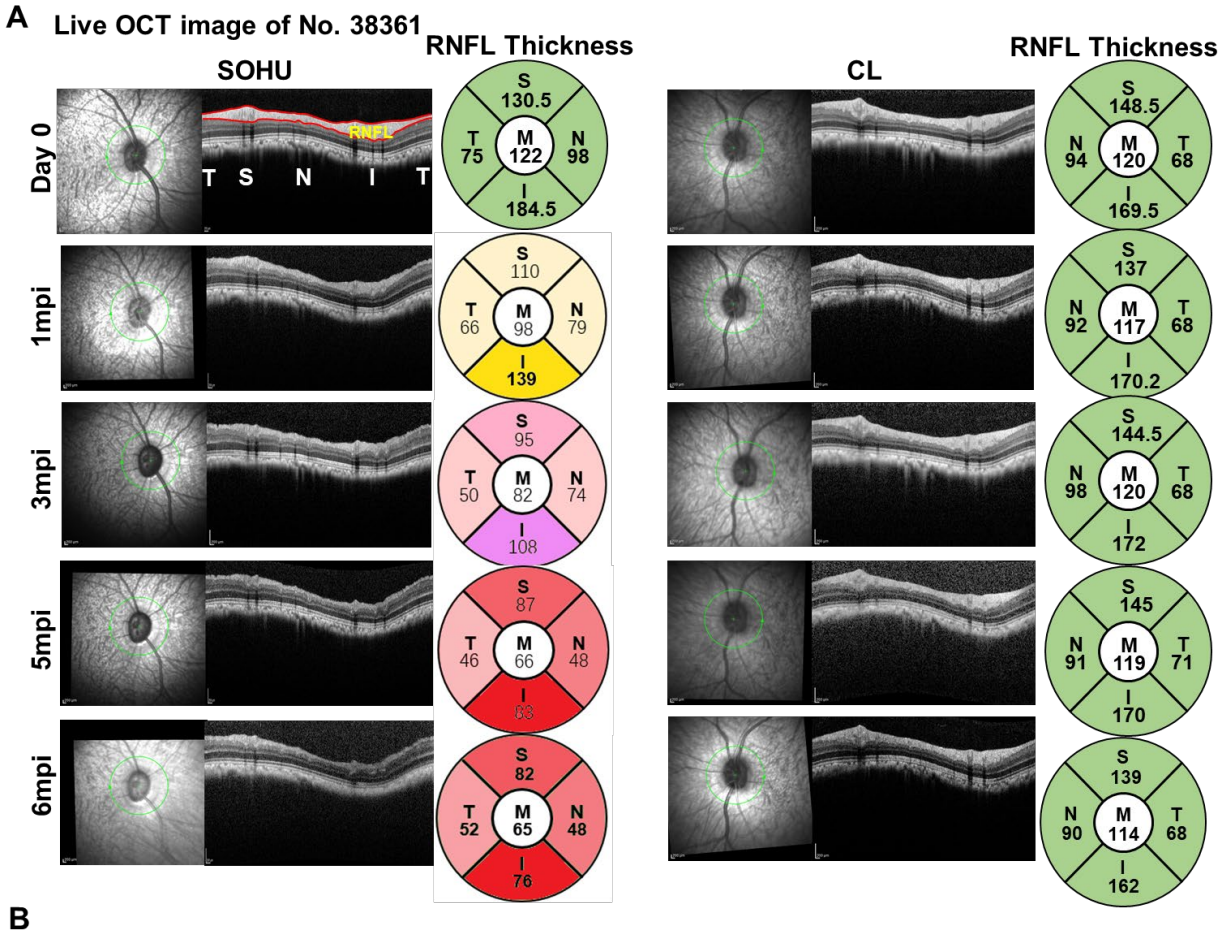

B

No. 38361	SOHU (μm)					CL (μm)				
	S	T	I	N	M	S	T	I	N	M
Baseline	131	75	185	98	122	149	68	170	94	120
1 Month	110	66	139	79	98	137	68	170	92	117
3 Month	95	50	108	74	82	145	68	172	98	120
4 Month	85	46	91	55	69	139	64	170	88	115
5 Month	87	46	83	48	66	145	71	167	90	118
1wk-Removal	90	50	85	50	69					
6 Month	82	52	76	48	65	139	68	162	90	114

Figure 3. Progressive quadrant-specific thinning of RNFL in SOHU eye of animal #38361 measured by peripapillary OCT. (**A**) Longitudinal SD-OCT imaging of macaque retina with a 12° peripapillary RNFL circle scan (green circle, 1536 A-scans per B-scan, ART>16 repetitions), and the illustration of the RNFL thickness at inferior (I), superior (S), nasal (N), and temple (T)

596 quadrants and the average/mean (M) over time. (**B**) Measurements of RNFL thickness at different

597 time points.

598 See also Figure 3-figure supplementary 1

599
600

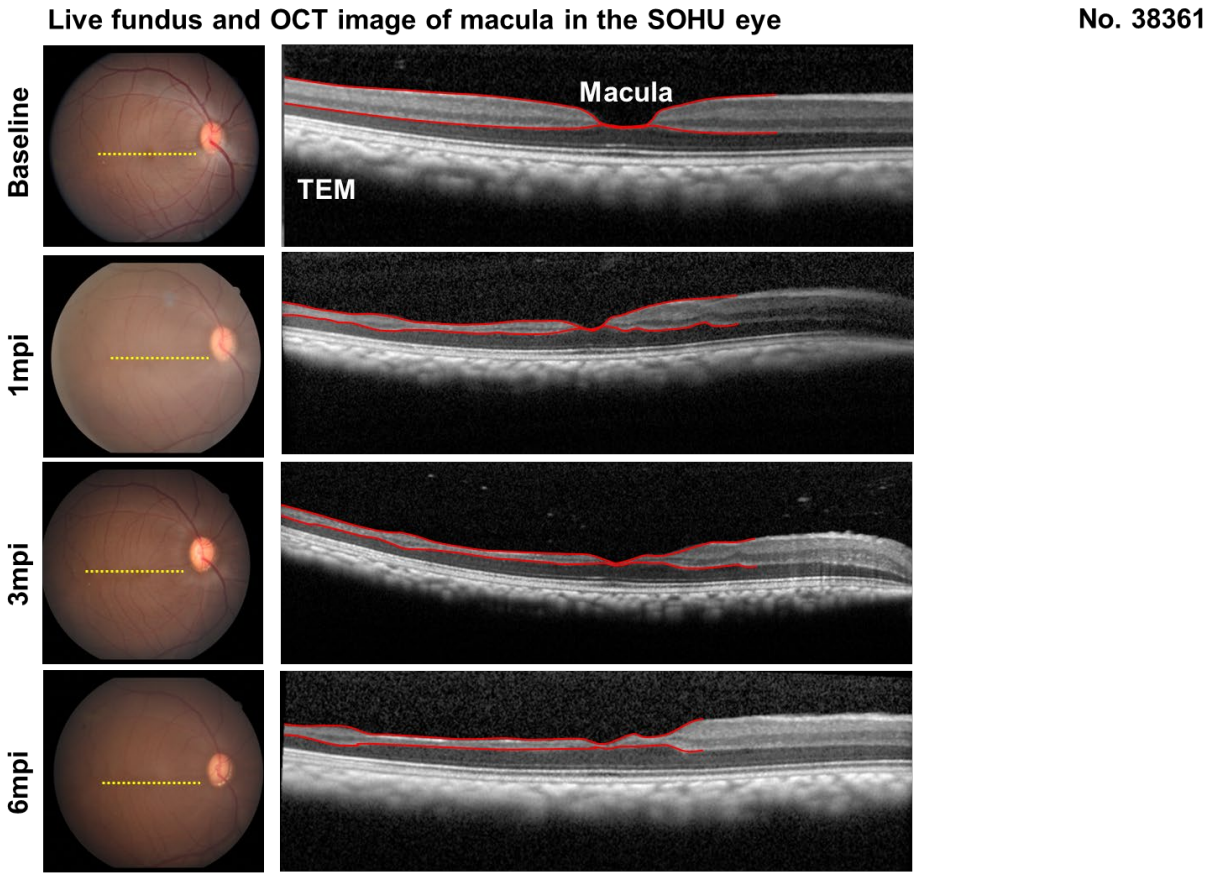

601

602 **Figure 3-figure supplementary 1. Retinal branch artery occlusion in macula of SOHU eye in**

603 **animal #38361.** The retinal fundus images and SD-OCT images of macula in the SOHU eye

604 before and after SO injection. Yellow dotted line outlines the OCT scanning area.

605

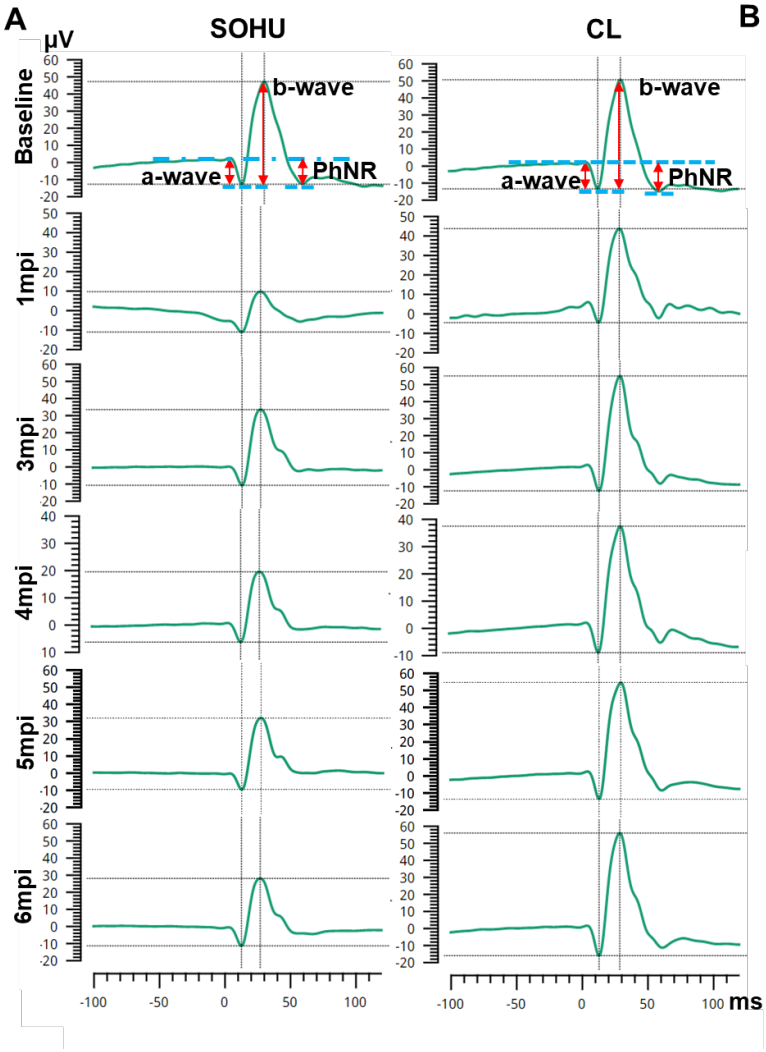

B

No. 38361 ERG (% of SOHU/CL)	a-wave	b-wave	PhNR
Baseline	95%	94%	88%
1mpi	80%	43%	51%
3mpi	86%	66%	31%
4mpi	71%	56%	29%
5mpi	71%	61%	33%
6mpi	71%	55%	39%

Figure 4. Visual function deficit in SOHU eye of animal #38361 measured by ERG. (**A**) Longitudinal ERG recording of macaque eyes at different time points. (**B**) Measurements of the amplitudes of a wave, b wave and PhNR, represented as percentage of SOHU eyes compared to CL eyes.

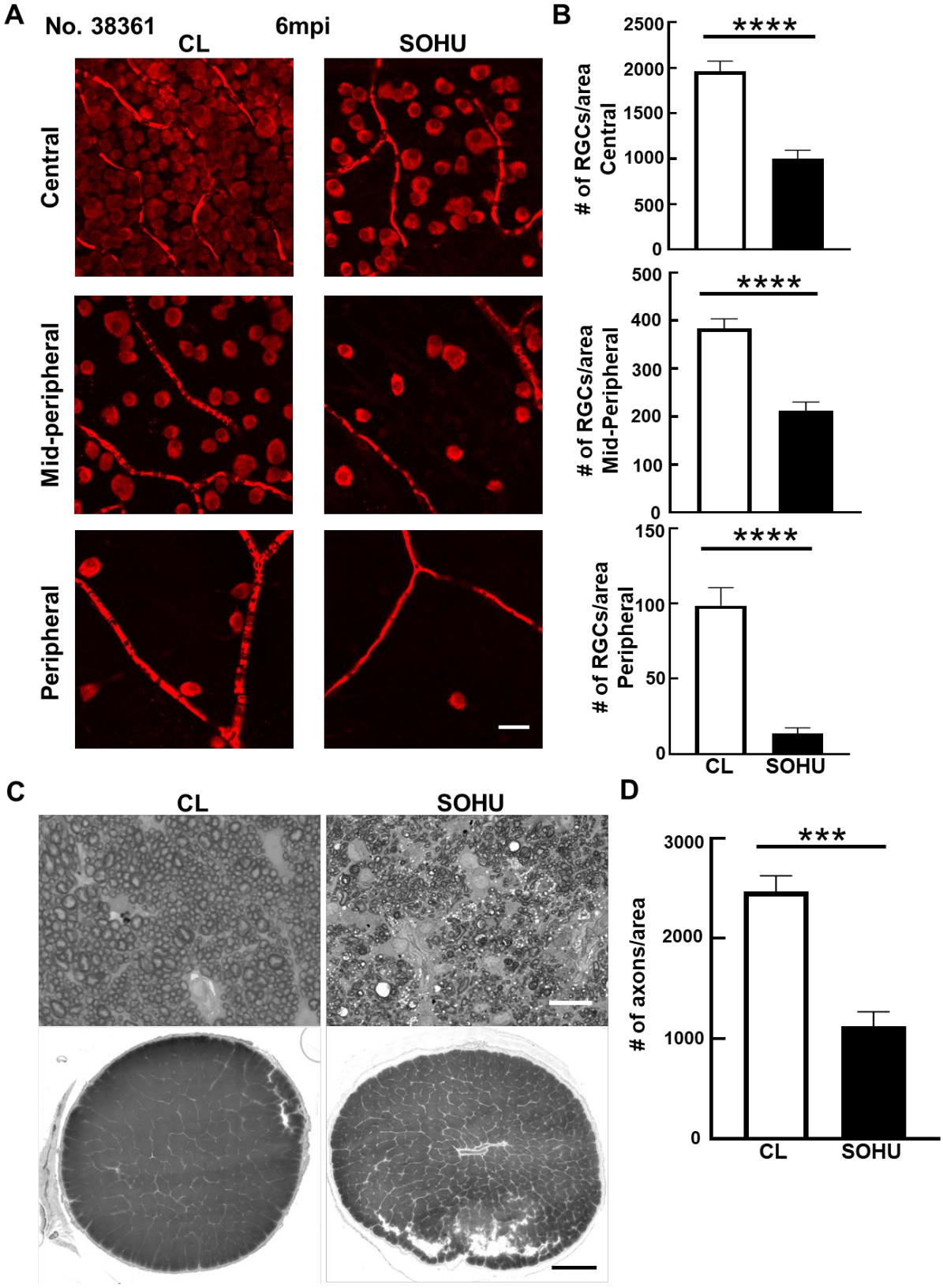
A
No. 38361
6mpi
CL
SOHU
Central
Mid-peripheral
Peripheral
B
****
# of RGCs/area
Central
2500
2000
1500
1000
500
0
****
# of RGCs/area
Mid-Peripheral
500
400
300
200
100
0
****
# of RGCs/area
Peripheral
150
100
50
0
CL
SOHU
C
CL
SOHU
D
***
# of axons/area
3000
2000
1000
0
CL
SOHU

614

615

616 **Figure 5. Severe RGC and ON degeneration in SOHU eye of animal #38361 at 6mpi.** (**A**)
617 Confocal images of wholemount retinas showing surviving RBPMS-positive (red) RGCs in the
618 peripheral, mid-peripheral, and central retina at 6mpi. Scale bar, 20 µm. (**B**) Quantification of
619 surviving RGCs in the peripheral, mid-peripheral, and central retina. Data are presented as means
620 ± s.e.m, ****: $P<0.0001$, Student's t-test. (**C**) Light microscope images of semi-thin transverse
621 sections of ON stained with PPD in the corresponding groups. Upper panel: 100 x, Scale bar, 20
622 µm; lower panel: 60 x, Scale bar, 500 µm. (**D**) Quantification of surviving RGC axons in ON. Data
623 are presented as means ± s.e.m, ***: $P<0.001$, Student's t-test.
624 See also Figure 5-figure supplementary 1

625

626

627

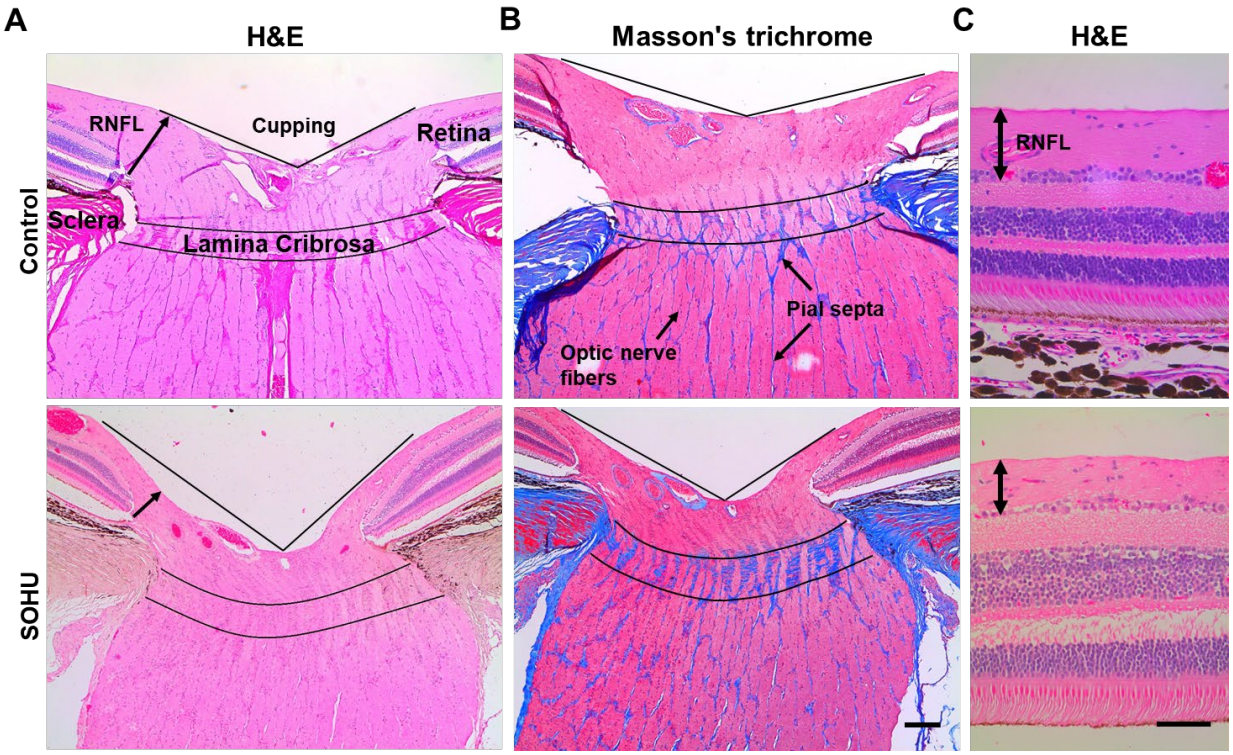

Figure 5-figure supplementary 1. ONH and retina sections in animal #38361. (**A**) ONH sections stained with H&E. (**B**) ONH sections stained with Masson's trichrome. Scale bar = 200 µm. (**C**) Retina sections stained with H&E. Scale bar = 50 µm.

A

SOHU	44876		45513		42946		44639		44193	
	SOHU	CL	SOHU	CL	SOHU	CL	SOHU	CL	SOHU	CL
Pre-Injection	15	18	13	12	9	9	13	12	11	14
Post-injection immediately	19	18	22	11	11	9	11	12	9	14
1mpi	4	16	Too low to read	14	6	11	8	17	5	11
2mpi	3	16	3	12	9	9	8	12	10	14
3mpi	2	11	3	11	8	9	8	16	12	14
4mpi					12	10	9	13	13	15
5mpi					9	6	8	12	12	11
6mpi					12	14	10	12	13	14

B

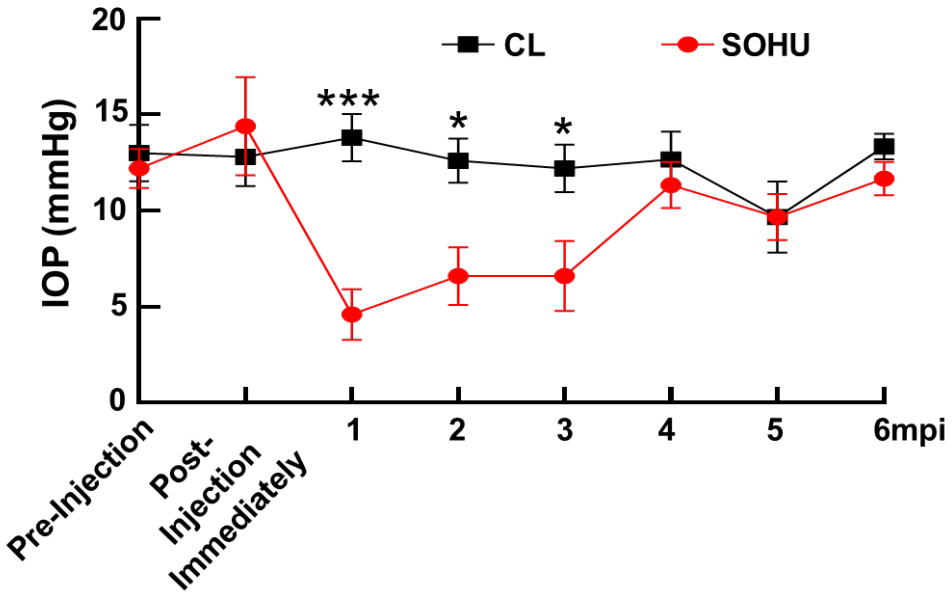

634

635

636 **Figure 6. Dynamic IOP changes of SOHU eyes in the other five animals.** Table (**A**) and (**B**)

637 ling graph presentation of longitudinal IOP measurements of experimental (SOHU) eyes and

638 contralateral control (CL) eyes at different time points after SO injection. mpi: month post
639 injection. Data are presented as means ± s.e.m, n = 5 (1-3mpi) and n = 3 (4-6mpi) of each group;
640 *: $p<0.05$, ***: $p<0.001$, Student's t test.

641
642
643

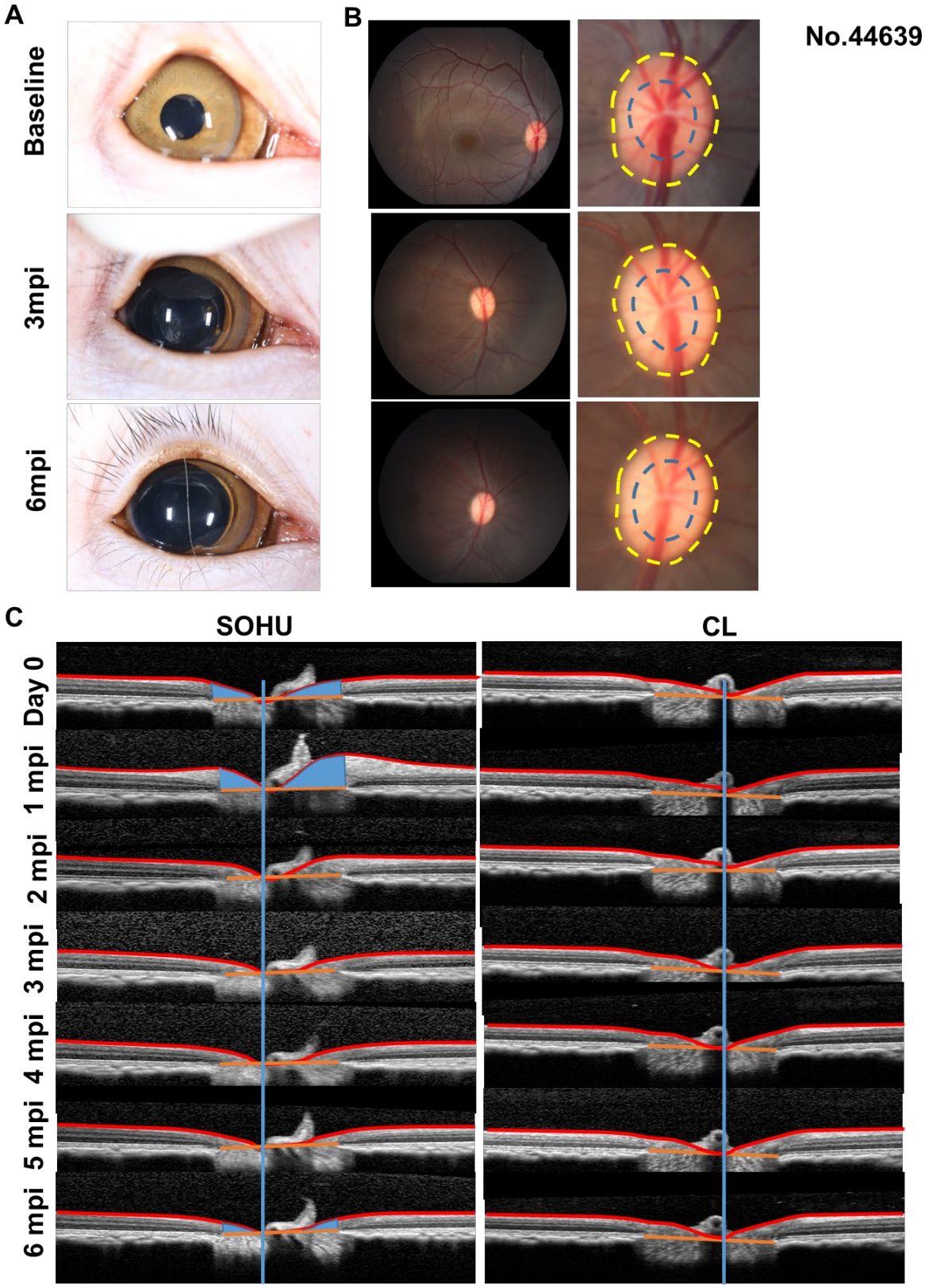
A
B
No.44639
Baseline
3mpi
6mpi
C
SOHU
CL
Day 0
1 mpi
2 mpi
3 mpi
4 mpi
5 mpi
6 mpi

644

645 **Figure 7. No detectable ONH "cupping" in the other five animals.** (**A**) Pupil dilation after SO
646 injection. (**B**) The retinal fundus images of the SOHU eye before and after SO injection. Yellow
647 dotted line outlines the optic disc; blue dotted line outlines optic cup. (**C**) Longitudinal SD-OCT
648 imaging of ON heads.

649
650
651

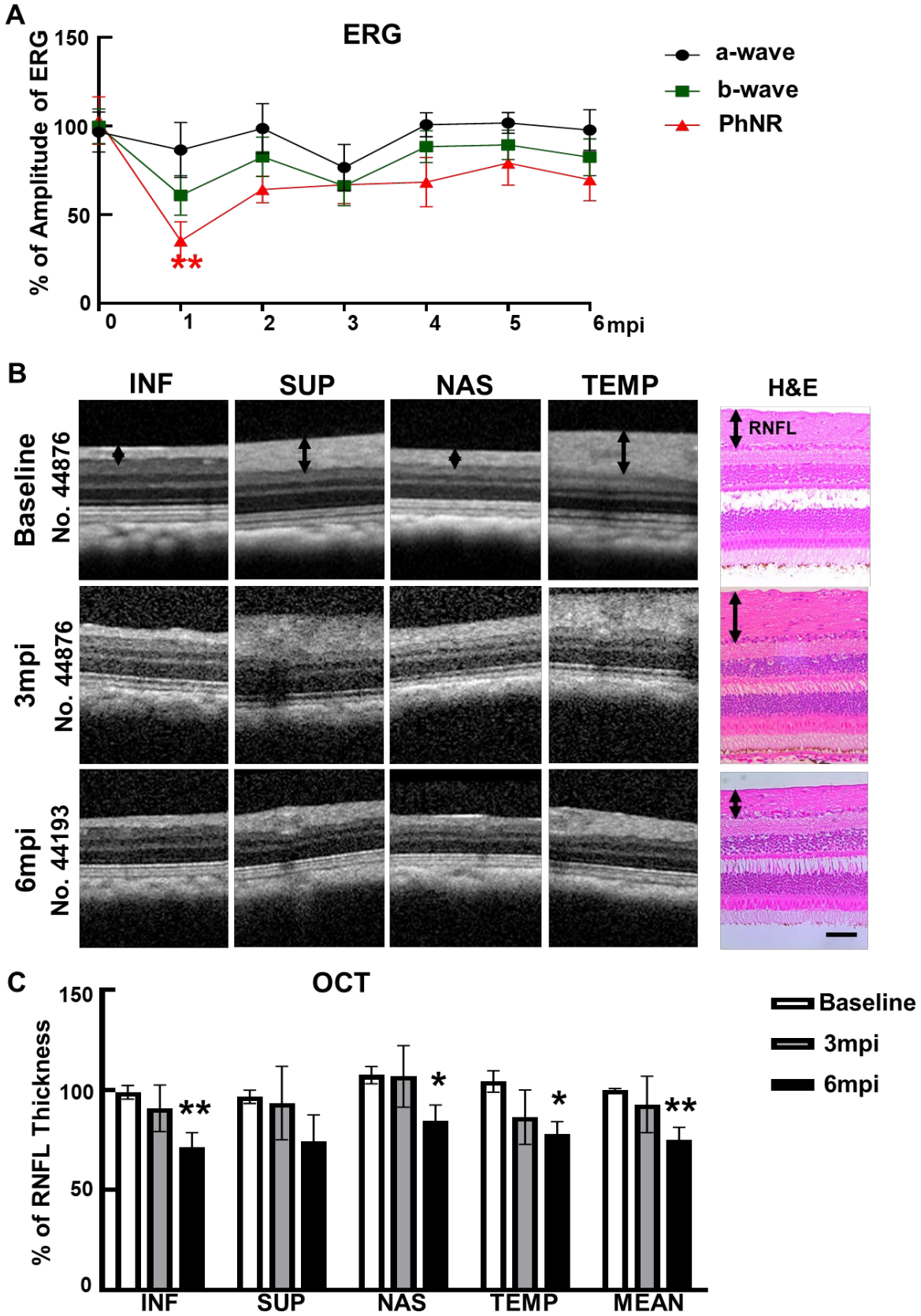
A
ERG
% of Amplitude of ERG
150
100
50
0
0
1
2
3
4
5
6mpi
**
a-wave
b-wave
PhNR
B
INF
SUP
NAS
TEMP
H&E
Baseline
No. 44876
3mpi
No. 44876
6mpi
No. 44193
RNFL
C
OCT
% of RNFL Thickness
150
100
50
0
**
*
*
**
INF
SUP
NAS
TEMP
MEAN
Baseline
3mpi
6mpi

652

653 **Figure 8. Visual function and morphological deficits of SOHU eyes in the other five animals.**
654 (**A**) Longitudinal ERG recording of macaque eyes at different time points after SO injection and
655 the measurements of the amplitudes of a wave, b wave and PhNR, represented as percentage of
656 the amplitudes in the SOHU eyes, compared to the CL eyes. (**B**) Longitudinal SD-OCT imaging
657 of SOHU retinas at inferior (I), superior (S), nasal (N), and temple (T) quadrants; and the H&E
658 staining of retina sections. (**C**) Measurements of RNFL thickness at different time points,
659 represented as percentage of SOHU eyes compared to CL eyes. Data are presented as means ±
660 s.e.m, n = 5 for 3mpi and n = 3 for 6mpi, *: $P<0.05$, **: $P<0.01$, Student's t test.
661
662
663

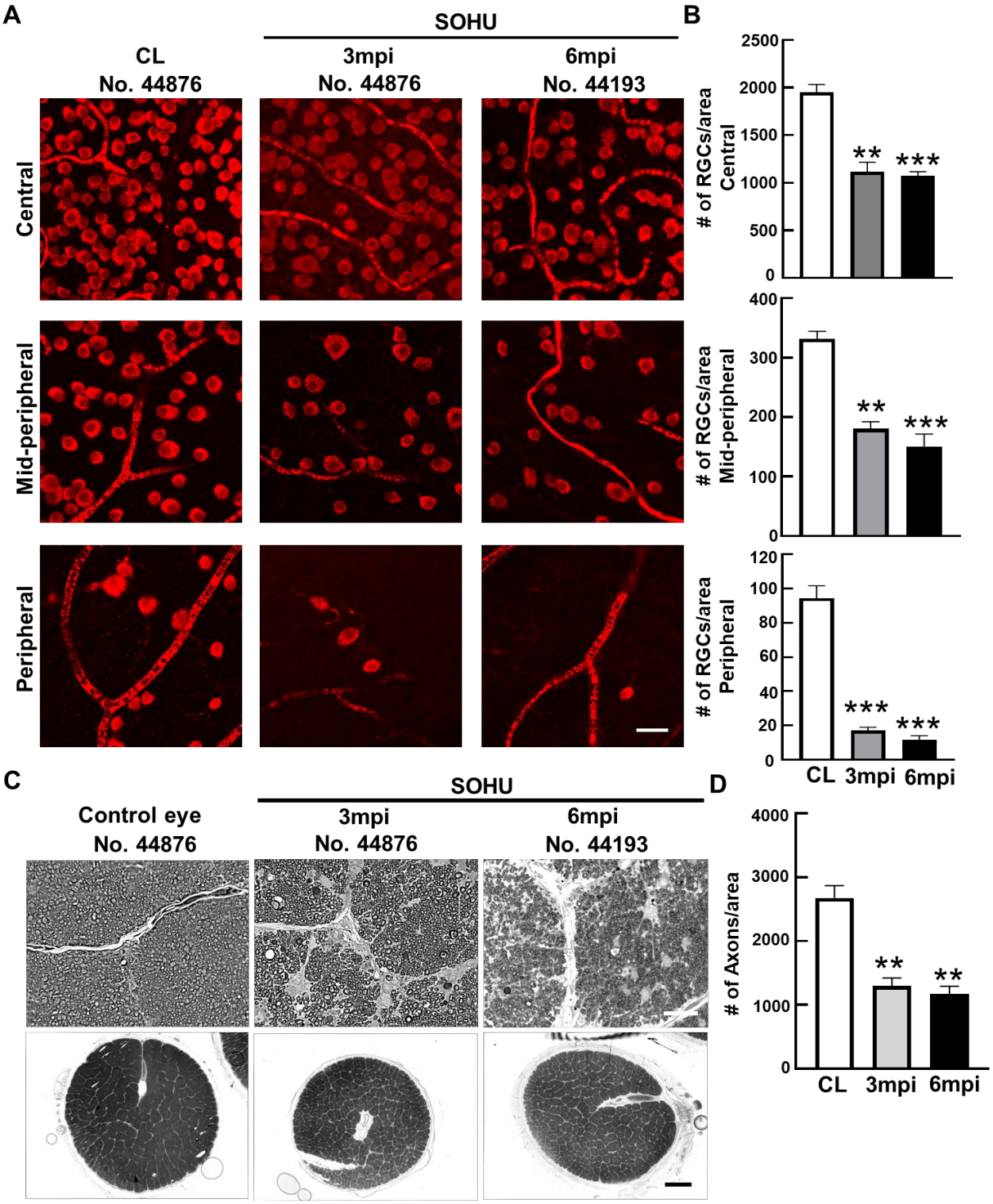

Figure 9. Severe RGC and ON degeneration in SOHU eyes at 3mpi and 6mpi. (**A**) Confocal images of wholemount retinas showing surviving RBPMS-positive (red) RGCs in the peripheral,

667 mid-peripheral, and central retina at 3and 6mpi. Scale bar, 20 µm. (**B**) Quantification of surviving
668 RGCs in the peripheral, mid-peripheral, and central retina. CL: contralateral control eyes. Data are
669 presented as means ± s.e.m, n = 2 for 3mpi and n = 3 for 6mpi, **: P<0.01, ***: P<0.001, one-
670 way ANOVA with Tukey's multiple comparison test. (**C**) Light microscope images of semi-thin
671 transverse sections of ON stained with PPD in the corresponding groups. Upper panel: 100 x, Scale
672 bar, 20 µm; lower panel: 60 x, Scale bar, 500 µm. (**D**) Quantification of surviving RGC axons in
673 ON. Data are presented as means ± s.e.m, n = 2 for 3mpi and n = 3 for 6mpi, **: *P*<0.01, One-
674 way ANOVA with Tukey's multiple comparison test.

675
676